Magnetic property enhancement of spinel Mn-Zn ferrite through atomic structure control

Jennifer Hölscher,[a] Michele Petrecca,[b,c] Martin Albino,[c] Pelle Gorm Garbus,[a] Matilde Saura-Múzquiz,[a,d] Claudio Sangregorio,[b,c] Mogens Christensen[a*]

[a] Center for Materials Crystallography, Department of Chemistry and Interdisciplinary Nanoscience Centre (iNANO), Aarhus University, Langelandsgade 140, DK-8000 Aarhus C, Denmark

[b] ICCOM-CNR, via Madonna del Piano 10, 50019 Sesto Fiorentino, Italy

[c] INSTM & Dept. of Chemistry "Ugo Schiff", via della Lastruccia 3 - 13, 50019 Sesto Fiorentino, Italy

[d] School of Chemistry, The University of Sydney, F11, Sydney, NSW, 2006, Australia

*Corresponding author: mch@chem.au.dk

Abstract

Temperature treatment of magnetic Mn-Zn ferrites with the composition $Mn_{0.6}Zn_{0.2}Fe_{2.2}O_4$ up to 1100 °C results in a tremendous enhancement of the saturation magnetization by more than 60%. Employing a robust combined Rietveld refinement of powder X-ray and neutron diffraction (PXRD and NPD) data, it is revealed how a reordering of the cations takes place during the annealing step, the extent of which depends on the annealing temperature. While Zn(II) exclusively occupies tetrahedral sites throughout the whole temperature range, as the annealing temperature increases up to 700 °C, the Mn(II) cation distribution shifts from 80(7)% of the total Mn content occupying the octahedral sites (partly inverse spinel) to Mn only being present on the tetrahedral sites (normal spinel). Above 700 °C, pronounced crystallite growth is observed, followed by an increase of the saturation magnetization. Complementary techniques such as energy dispersive X-ray spectroscopy (EDS) and transmission electron microscopy (TEM) confirm an even cation distribution and the particle growth with annealing temperature. The structural changes caused by annealing of spinel ferrites directly alter the magnetic properties of the materials, thus serving as an easy handle for enhancing their magnetic properties.

Introduction

Magnetic nanoparticles are key components in many novel technological applications, such as MRI contrast agents,[1,2] hyperthermia cancer therapy,[3] targeted drug delivery,[4] catalysis,[5] miniaturization of electronic equipment,[6] and exchange-spring magnets.[7,8]

In the cubic spinel ferrites of the general formula MFe_2O_4, *M* being a divalent transition metal *e.g.* Mn^{2+}, Fe^{2+}, Co^{2+}, Ni^{2+}, Zn^{2+}, *etc.*, the cations are distributed on sites with tetrahedral (A sites) or octahedral coordination (B sites), as shown in Figure 1. The magnetic moments of the cations are coupled through super-exchange interactions, giving rise to ferromagnetic coupling between sites of equal geometry (*i.e.* A-A and B-B) and antiferromagnetic coupling between octahedral and tetrahedral sites (*i.e.* A-B). This coupling results in a net ferrimagnetic structure, given that there are twice as many B sites as A sites. The material's magnetic performance is determined by the composition and the distribution of the cations over the two crystallographic sites. In a so-called normal spinel, the divalent cations occupy the tetrahedral A sites, while Fe(III) occupies the octahedral B sites. In an inverse spinel, however, the divalent atoms occupy the octahedral sites, forcing half of the Fe(III) cations onto the tetrahedral sites. Intermediate structures are also possible, described by the inversion degree δ as given by $[M(II)_{1-\delta}\ Fe(III)_{\delta}]^{A}\ [M(II)_{\delta}\ Fe_{2-\delta}]^{B}O_4$. Given the ferrimagnetic nature of the compound, non-magnetic cations occupying tetrahedral sites will in principle increase the saturation magnetization of the compound, as will strongly magnetic cations occupying octahedral sites. This has been proven to happen when partially substituting non-magnetic Zn(II) into the A site.[9] However, such increase in saturation is only achievable up to a certain substitution degree, above which the aforementioned super-exchange interactions are disrupted by the non-magnetic cation, causing an antiferromagnetic coupling between the octahedral sites.[10–13]

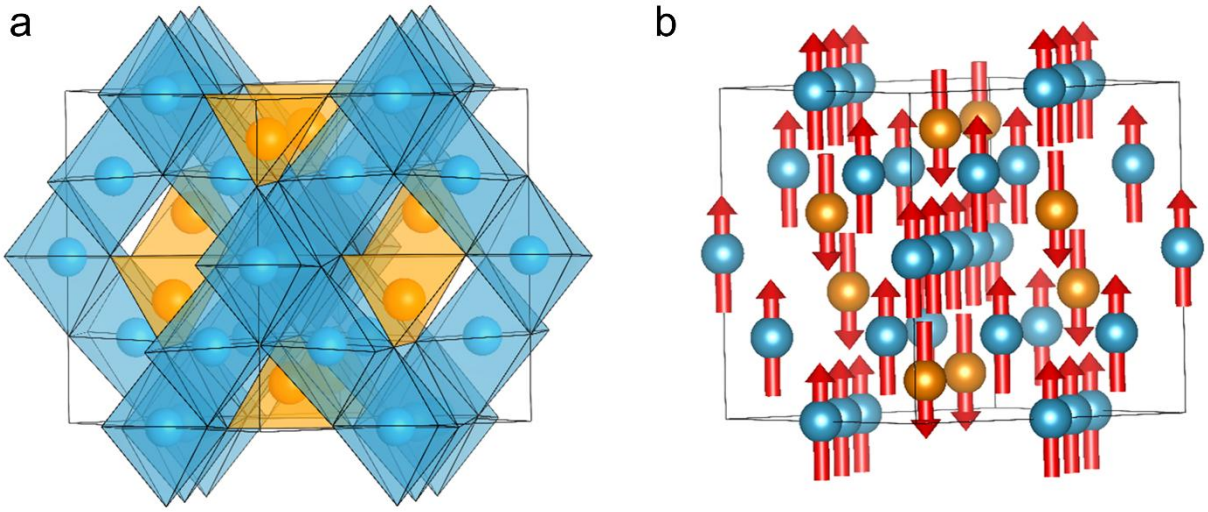

Figure 1: (a) Crystal structure of the cubic spinel (space group Fd-3m). Blue: octahedral sites, orange: tetrahedral sites. The oxygen atoms are not shown, but are found in the vertices of the polygons. (b) Coupling scheme of magnetic moments in a cubic spinel. Figures made with the program VESTA.[14]

$Mn_{1-x}Zn_xFe_2O_4$ nanoparticles have recently received much attention because high saturation magnetization (M_s) values up to *ca.* 127 Am^2kg^{-1} (175 Am^2kg^{-1} if only the magnetic atoms are taken into account) have been reported.[1] Typical values of M_s in the literature generally differ strongly from this value, displaying

values typically ranging between 23 and 85 Am^2kg^{-1}.[15–17] The wide range of values in the literature can be attributed to modifications of microstructure and cation distribution. Despite these characteristics being key to explaining the differences in the magnetic performance of Mn-Zn substituted spinel ferrites, there is a general lack of investigations addressing the microstructure and cation distribution. This is partly because the cation distribution effect is particularly difficult to unravel in the case of neighboring atoms in the periodic table when using laboratory X-rays or a standard synchrotron experiment. Even though powder X-ray diffraction (PXRD) allows modeling the site occupancies of all cations in the crystallographic structure, the reliability of a model is compromised when elements are in the vicinity of each other in the periodic table. This is a challenge in complex spinel ferrites, as the transition metals have a similar number of electrons and therefore similar atomic form factors, *e.g.* Mn (Z = 25) and Fe (Z = 26). A way to circumvent this is to collect neutron powder diffraction (NPD) data. When using NPD, strong contrasts between cations can be achievable, as the scattering lengths vary erratically with atomic number, *e.g.* Mn (b_{Mn} = -3.73 fm) and Fe (b_{Fe} = 9.45 fm). This facilitates modeling the cation distribution in spinel ferrites reliably.

The cation distribution of a sample depends on the crystal field stabilization energies of the individual cations, their charge and their ionic radius.[18] Annealing can introduce changes in the cation distribution. However, not only the heating step is decisive in modifying the cation distribution, but also the cooling procedure is crucial in controlling it and thereby obtaining the desired configuration.[19] Unfortunately, many studies in the literature do not report the cooling procedure after the annealing step,[16,20,21] which makes the comparison between studies difficult, if not meaningless.

Zn in $ZnFe_2O_4$ is typically reported to only occupy tetrahedral sites, while Mn in $MnFe_2O_4$ is distributed over tetrahedral and octahedral sites, with an inversion degree of 20% in bulk samples.[10,22,23] However, the cation distribution can differ due to synthesis strategy, heating treatment and crystallite size.[12,13,19,23–26] Quenching $MnFe_2O_4$ after annealing leads to a more inverse material,[27,28] while slow cooling of $ZnFe_2O_4$ leads to the thermodynamically stable configuration with Zn solely occupying the tetrahedral sites, *i.e.* a normal spinel.[29] Existing studies dealing with as-prepared $Mn_{1-x}Zn_xFe_2O_4$ yield inconsistent results, such as Zn only occupying tetrahedral sites, while Mn and Fe are partly inverse,[30,31] both Zn and Mn in a fully normal distribution, with Fe only on octahedral sites,[32] or Mn and Fe occupying only octahedral sites, while Zn is at high Zn contents partly inverse.[33] However, some of the existing reports deduce the cation distribution from the lattice parameters[31] or the relative intensities of individual PXRD peaks[33], which are not reliable descriptions as both are affected by a number of parameters and not just the cation distribution, especially in the case of nanoparticles. Even though it is known that temperature treatments

affect the cation distribution,[19] to our knowledge, the effect of an annealing treatment of the cation distribution in $Mn_{1-x}Zn_xFe_2O_4$ has not been reported so far.

In this study, we report changes of microstructure and cation distribution of $Mn_{0.6}Zn_{0.2}Fe_{2.2}O_4$ nanoparticles synthesized by a co-precipitation method and subsequently subjected to heat treatment at temperatures up to 1100 °C in a nitrogen atmosphere. The annealing is followed by a controlled cooling (approximately 5 K min^{-1} above 700 °C and 1 K min^{-1} below 700 °C). Microstructural properties and cation occupancies were extracted from combined Rietveld refinements of PXRD and NPD datasets. Moreover, the magnetic properties of the obtained samples were characterized using a SQUID. It is observed that a redistribution of Mn and Fe occurs at temperatures up to 700 °C, after which the cations do not migrate to different sites and a pronounced grain growth begins. After annealing at 1100 °C, the saturation magnetization is increased by *ca*. 62% to a value of 95(1) Am^2kg^{-1}.

The results shine light on the effects of annealing followed by controlled cooling, with focus on the redistribution of cations and changes in the microstructure. Even for a given composition, tremendous differences in the magnetic properties are possible, depending on heat treatment. This has to be taken into account when tailoring new synthesis techniques for enhanced magnetic performances of complex spinel ferrites.

Experimental

Sample preparation

Iron(III) chloride hexahydrate ($FeCl_3 \cdot 6H_2O$, 98%, Sigma-Aldrich), manganese(II) chloride tetrahydrate ($MnCl_2 \cdot 4H_2O$, 98%, Sigma Aldrich), zinc(II) chloride ($ZnCl_2$ 98%, Sigma Aldrich), sodium hydroxide (NaOH, Sigma Aldrich) were used without any further purification.

$Mn_{0.6}Zn_{0.2}Fe_{2.2}O_4$ nanoparticles were synthesized using a co-precipitation method, where 500 mL of demineralized (DM) H_2O was degassed with N_2 flow for one hour. 8.70 g of NaOH (0.217 mol) were solubilized in 450 mL of degassed DM H_2O and heated to 100 °C. 14.86 g of $FeCl_3 \cdot 6H_2O$ (0.055 mol), 2.96 g of $MnCl_2 \cdot 4H_2O$ (0.015 mol) and 0.68 g of $ZnCl_2 \cdot$(0.005 mol) were dissolved in 50 mL of degassed DM H_2O and added to the alkaline solution at 100 °C, under vigorous stirring and N_2 flow. Immediately, a black precipitate formed and the black slurry was kept at reflux for 2 h under magnetic stirring; then, it was cooled to room temperature. The resulting black powder was separated by using an external magnet, washed several times with water, ethanol and acetone and finally dried under nitrogen flow, obtaining ca. 5.5 g of a black powder (ca. 95% yield). The obtained nanoparticles were subsequently annealed at 500 °C, 700 °C, 900 °C and 1100 °C in a tubular furnace (Elite TSH 15/75/610) in N_2 atmosphere. The samples, each

consisting of ca. 1 g of nanopowder, were heated at 10 K min^{-1} up to the target temperature, left for 2 h and then cooled at 5 K min^{-1} down to 700 °C and from there at 1 K min^{-1} to room temperature.

Powder diffraction experiments

PXRD measurements were conducted on a Rigaku SmartLab diffractometer equipped with a Cu Kα anode and a Ge(111) monochromator producing a wavelength of 1.5406 Å. The patterns were collected in Bragg-Brentano geometry with a D/tex Ultra 250 strip detector in fluorescence suppression mode in the angular 2θ range between 15° and 110°.

NPD patterns were collected at the DMC instrument, SINQ, PSI, Switzerland, using a wavelength of 2.4576 Å and angular range of 2θ = 13-93°,[34] and at the D1B instrument, ILL, France, with λ = 2.5200 Å in the range of 2θ = 0.7-129°.[35,36]

All PXRD measurements were conducted at room temperature.

Rietveld refinement

The diffraction data were analyzed with Rietveld refinements using the software package *FullProf suite*.[37] The intrinsic broadening parameters of the instruments were described using instrumental resolution files (*.irf*). The parameters were determined from the refinement of powder diffraction data of a suitable calibrant measured under identical conditions as the sample. The peak profile was described using the Thompson-Cox-Hastings formulation of the pseudo-Voigt function. The background was for both PXRD and NPD data described with a Chebyshev polynomial. Parameters refined for each phase were the scale factors, lattice parameters, oxygen positions, Debye-Waller factors and the zero-point offset. The Debye-Waller factor was constrained for all atoms, patterns and phases to the same value, while the lattice parameters and oxygen positions were constrained for each phase individually. The Lorentzian peak broadening parameter, *Y*, was used for extracting the nanosize of the crystallites. As this parameter is wavelength-dependent, a constrain reflecting the ratios of the individual wavelengths of the different collected patterns was applied. The magnetic moment of each magnetic ion on the tetrahedral and octahedral sites was constrained to the same absolute value with different signs, thus yielding an average magnetic moment for the sites.

All refined values can be found in Tables S1 and S2 in the Supporting Information.

Microscopy

Transmission electron microscopy images were taken using a FEI TALOS F200X scanning/transmission electron microscope (S/TEM) with a resolution of 0.12 nm, equipped with a X-FEG electron source, a constant-power X-TWIN objective lens, and a Ceta 16M pixel CMOS camera with a read-out speed of 25 fps

at 512x512. The brightness of the X-FEG was $1.8*10^9$ $Acm^{-2}srad$ at 200 kV. The total beam current was >50 nA, while the probe current was 1.5 nA for a 1 nm probe (200 kV). Scanning transmission electron microscopy images were taken with the same instrument, using a high-angle annular dark field detector (HAADF) with a resolution of 0.16 nm, an EDX solid angle of 0.9 srad and an inner acceptance angle of 50.96 mrad. For the elemental maps, a Super-X EDS detector was used (4 SDD symmetric design, windowless, shutter-protected). The energy resolution was ≤136 eV for Mn *K*α and 10 kcps (output).

Magnetic measurements

Hysteresis loops were recorded at room temperature on tightly randomly packed powder samples, using a Quantum Design MPMS superconducting quantum interference device (SQUID) magnetometer. The maximum field applied was ±5 T. Saturation magnetization values were extracted from the hysteresis loops using the law of approach to saturation.[38]

Results and discussion

Phase identification

The PXRD diffractograms reveal that all samples mainly consist of a spinel phase (space group *Fd-3m*), indicating the formation of $Mn_{0.6}Zn_{0.2}Fe_{2.2}O_4$ (Figure 2), with the corresponding magnetic phase also being present in the NPD patterns (Figure 3). While the as-prepared sample and the one annealed at 500 °C consist of phase-pure spinel ferrite, the samples annealed at 700 °C and 900 °C contain each 24.3(4) and 27.0(4) wt.% α-Fe_2O_3 (hematite, space group *R*-3*c*), while annealing at higher temperatures (1100 °C) decreases the α-Fe_2O_3 content to < 1 wt.%.

STEM-HAADF images were taken of as-prepared samples and samples annealed at 1100 °C to confirm the compositions and to inspect the elemental distribution. The cations appear in both cases to be evenly distributed within the crystallites (Figure 4, additional images in Figures S4 and S5 in the Supporting Information). The compositions extracted from the STEM-X EDS analysis are close to the nominal ones, with the as-prepared samples having cation ratios of Mn/Zn/Fe of 0.64/0.24/2.13, while the sample annealed at 1100 °C was found to have the stoichiometry 0.64/0.22/2.15. Results from STEM-HAADF and related errors can be found in Tables S3-S6 in the Supporting Information. The differences in cation concentration are approximately within the error of *ca*. ±10%.

In the literature, it has previously been reported that hematite appears and disappears during the annealing of $Mn_{0.5}Zn_{0.5}Fe_2O_4$ in air or oxygen-rich atmospheres, while forming a Mn-rich spinel.[39,40] It was argued that this process is controlled by the oxygen partial pressure.[39,40] Hematite appearing during the annealing in N_2 in this study may possibly be explained by OH^- from the synthesis being adsorbed on the

crystallites. Upon annealing, it may be released, causing an increasing oxygen content in the annealing atmosphere. However, the exact processes occuring during the annealing of $Mn_{0.6}Zn_{0.2}Fe_{2.2}O_4$ are outside the scope of this study.

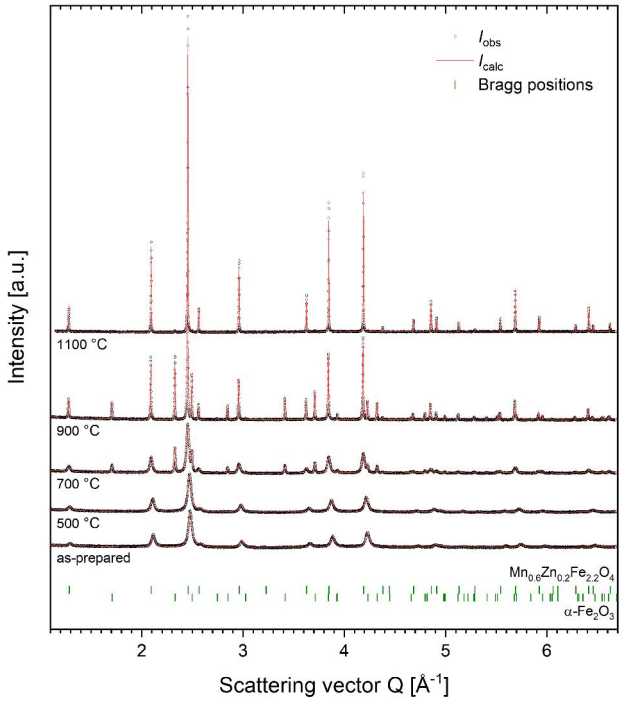

Figure 2: PXRD diffractograms measured with Cu Kα_1 radiation. The indicated temperature is the annealing temperature, from which the $Mn_{0.6}Zn_{0.2}Fe_{2.2}O_4$ samples were cooled in a controlled way. The patterns are depicted in arbitrary units, with individual offsets, but with the same y-axis scaling for all patterns to reflect the differences in observed peak intensity.

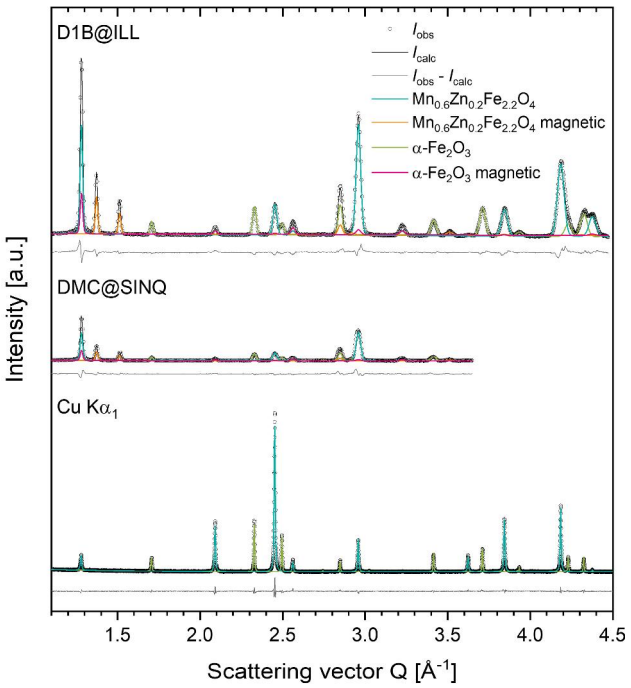

Figure 3: Overview of the diffractograms of the sample annealed at 900 °C, as representative of the whole series. From bottom to top: in-house (Cu Kα), DMC@SINQ, and D1B@ILL. Diffractograms of other samples can be found in Figure S1 in the Supporting Information.

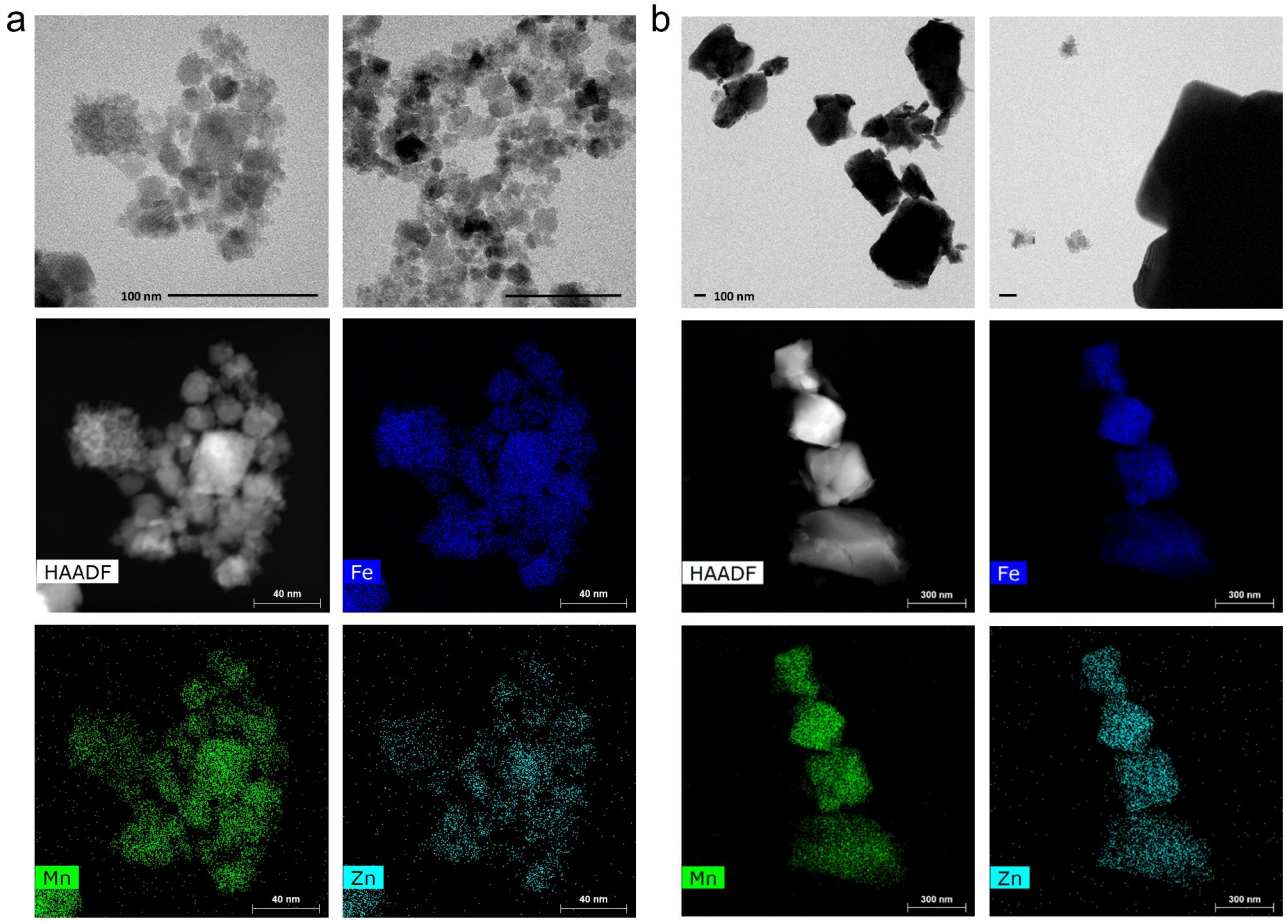

Figure 4: TEM and EDS images of (a) as-prepared and (b) annealed (1100 °C) $Mn_{0.6}Zn_{0.2}Fe_{2.2}O_4$. The scalebar in the TEM images is 100 nm for all samples, while the scalebar on the HAADF and elemental mapping images of the as-prepared sample is 40 nm and of the annealed sample 300 nm. Additional TEM and EDS images can be found in Figures S2-S5 in the Supporting Information.

Peak profile

Samples annealed at temperatures up to and including 900 °C exhibit peak broadening exceeding instrumental broadening which indicates that the crystallites are on the nanoscale.

The lattice parameter of the spinel phase expands for samples annealed at up to 900 °C and shrinks slightly when the annealing takes place at 1100 °C (Figure 5a). The oxygen positions follow a similar trend, with respect to their displacement away from the ¼ position (Figure 5a). The oxygen position shifting away from (¼, ¼, ¼) indicates that tetrahedral sites expand, while octahedral sites are compressed. This expansion/contraction of the coordination polyhedra would take place in the case of cation movement, with a larger cation migrating from the octahedral site onto the tetrahedral site.[18] This topic will be discussed further under Cation distribution.

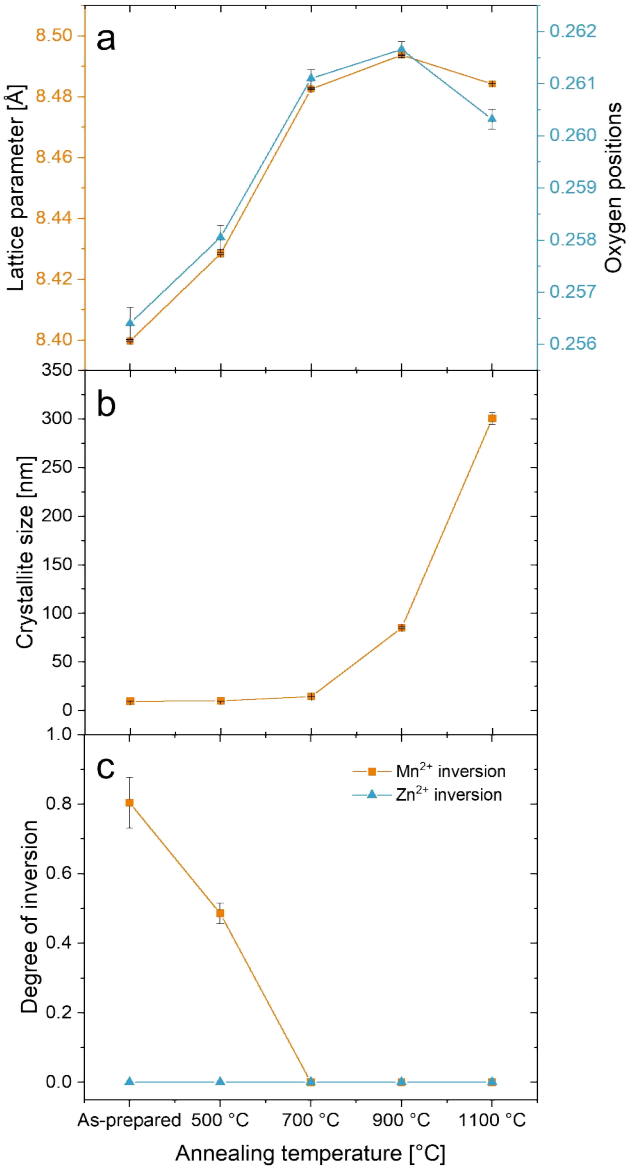

Figure 5: Microstructural properties extracted from the Rietveld refinements. (a) Lattice parameters and oxygen positions, (b) crystallite size, the value of the sample annealed at 1100 °C is out of resolution, so the absolute crystallite size cannot be determined reliably, (c) degree of inversion of Mn(II) and Zn(II). The exact refined values can be found in Tables S1 and S2 in the Supporting Information.

Crystallite size

The Scherrer equation was used to calculate the crystallite sizes, using the extracted peak broadening parameters from the refined model, taking instrumental broadening into account (Figure 5c). The values for the crystallite sizes can be found in Table 1. Only limited crystal growth in $Mn_{0.6}Zn_{0.2}Fe_{2.2}O_4$ occurs up to 700 °C, after which the crystallite size increases steeply. The crystallite size after annealing at 1100 °C is above the instrumental resolution limit, so that the absolute crystallite size cannot be determined. The α-

Fe_2O_3 crystallites are 40.5(7) nm large when the phase is first detected after annealing at 700 °C, but grow to 148(4) nm after annealing at 900 °C.

Table 1: Compositions, structural and magnetic properties of all samples. Values marked with a star (*) were fixed. The value of the crystallite size of the sample annealed at 1100 °C (marked with ‡) is above the resolution limit of the instruments for crystallite size determination. For a more detailed overview, including the exact site occupancies, please refer to Tables S1 and S2 in the Supporting Information.

Annealing temperature [°C]	**α-Fe_2O_3 content [wt.%]**	**Lattice parameter [Å]**	**Oxygen displacement**	**Crystallite size [nm]**	**Mn(II) inversion [%]**	**$M_{s,\ SQUID}$ [Am^2kg^{-1}]**
As-prepared	-	8.3956(2)	0.2564(3)	9.55(6)	80(7)	59(1)
500	-	8.4242(2)	0.2581(2)	10.00(7)	49(3)	62(1)
700	24.3(4)	8.4826(1)	0.2612(2)	14.45(9)	0*	60(1) (79(1) for a pure ferrite)
900	27.0(4)	8.49365(5)	0.2617(2)	81.1(8)	0*	57(1) (79(1) for a pure ferrite)
1100	<1	8.48419(3)	0.2603(2)	bulk‡	0*	95(1)

TEM images of as-prepared samples show a wide particle size distribution with most particles exhibiting sizes between 3 and 25 nm. After annealing at 1100 °C, significant particle growth has occurred and the particle size distribution is broad, with agglomerated particles up to 2 µm and small particles with sizes mostly between 10 and 100 nm.

Cation distribution

A combined Rietveld refinement of the PXRD and the NPD patterns was performed to extract the cation occupancies, distribution and inversion degree. In phase-pure samples, the crystallographic sites were assumed fully occupied, while in the hematite containing samples, the Fe content was allowed to vary on both tetrahedral and octahedral sites. In the first approach, all cations were allowed to occupy both tetrahedral and octahedral sites. The refinement of Zn occupancies on octahedral sites led to negative values close to zero. As a consequence of this result, Zn was eventually fixed in all samples to occupy only tetrahedral sites. Likewise, Mn was fixed to tetrahedral sites in samples annealed at 700 °C, 900 °C and 1100 °C. Fe(II) is expected to occupy the octahedral sites due to lower crystal field splitting energies, however it is not possible to follow the potential change in oxidation state.

The results from the Rietveld refinements show that cation reordering takes place below 700 °C (Figure 5c). Given that the cation redistribution takes places at temperatures where no significant crystallite growth has occured, such a redistribution must be due to the temperature treatment and independent of the crystallite size.

In the as-prepared samples, Zn occupies tetrahedral sites exclusively, while Mn is 80(7)% inverse, *i.e.* 80(7)% of the Mn in the sample occupies octahedral sites. The annealing causes Mn to move towards the tetrahedral sites, while Zn stays unchanged on the tetrahedral sites (Figure 5c). After annealing at 700 °C, all Mn is located on tetrahedral sites and the cation distribution does not change further when annealed at higher temperatures. Moreover, the formation of the α-Fe_2O_3 phase leads to a reduction of the Fe content of the spinel phase in samples annealed at 700 and 900 °C, especially on octahedral sites.

The observed changes of the oxygen positions corroborate these findings as the relatively larger Mn(II) moves from octahedral sites (83 pm) to tetrahedral sites (66 pm),[41] swapping positions with Fe(III) (49 pm in tetrahedral, 65 pm in octahedral sites)[41]. This cation reordering also explains the observed increase in unit cell size.

The site Mn occupies in spinel ferrites has been shown to vary depending on the synthesis conditions. Samples prepared by co-precipitation techniques have previously been observed to be more inverse than the 20% inversion typically reported for bulk samples prepared by solid state synthesis methods.[21] Inversion degree studies of non-substituted $MnFe_2O_4$ spinels show that annealing in vacuum and inert gases yield a more normal distribution of Mn,[21,42] whereas annealing in air causes Mn to become more inverse.[21,27,43] The study presented here confirms that the Mn redistribution in $Mn_{0.6}Zn_{0.2}Fe_{2.2}O_4$ in a N_2 atmosphere corresponds to that of the non-substituted Mn-spinel, $MnFe_2O_4$. The oxidizing/non-oxidizing nature of the annealing environment seems to be the determining factor for the cation movement. Judging from the redistribution to tetrahedral sites, Mn(II) stays in a divalent oxidation state, as Mn(III) prefers octahedral sites due to its crystal field stabilization energy.[18,42] This matches reports that the redistribution of Mn to octahedral sites is accompanied by an oxidation to Mn(III) when annealing in air.[21,27,43] The oxidation to Mn(III) observed in those studies may in fact be the driving force for the Mn migration, forcing it onto the more favorable octahedral sites. These results underline the importance of the annealing atmosphere for controlling the magnetic performance of Mn-containing spinel ferrites.

In the case of Zn, literature studies show that Zn in $Ni_{1-x}Zn_xFe_2O_4$ is actually partly inverse (up to 28%), increasingly migrating towards tetrahedral sites during annealing in air.[12,23] In the present study, however, Zn exclusively occupies the tetrahedral sites already in the as-prepared material. This illustrates that cation occupancies cannot be deduced from the cation occupancy in compounds with a different composition of cations, but that the individual cations affect each other regarding sites preferences.

Magnetic properties

Field-dependent magnetization measurements show that within the accuracy limit of the measurement, (± 0.2 kA m^{-1}), there is no coercivity or remanence of the samples at room temperature, in agreement with

the soft character of the Mn-Zn ferrite. The saturation magnetization of the samples is approximately constant within the error at annealing temperatures up to 900 °C (Figure 6a, full hysteresis curves in Figure S6 in the Supporting Information). However, for the samples annealed at 700 °C and 900 °C, the α-Fe_2O_3 content (up to 27.0(4) wt.%) must be taken into account, as it is antiferromagnetic and therefore reduces the overall mass magnetization. Superparamagnetic behaviour of α-Fe_2O_3 is not expected because the crystallites are too large (40.5(7) and 148(4) nm for the samples annealed at 700 °C and 900 °C, respectively). A corrected M_s representing only the spinel ferrite phase was calculated for those samples, assuming the contribution of hematite to be negligible (M_s values of 0.25 Am^2kg^{-1} can be found in the literature for α-Fe_2O_3)[44] and no magnetic interaction between the phases. This results in M_s values of 79(1) Am^2kg^{-1} for both samples. The highest M_s value was reached after annealing at 1100 °C, yielding a M_s of 95(1) Am^2kg^{-1}.

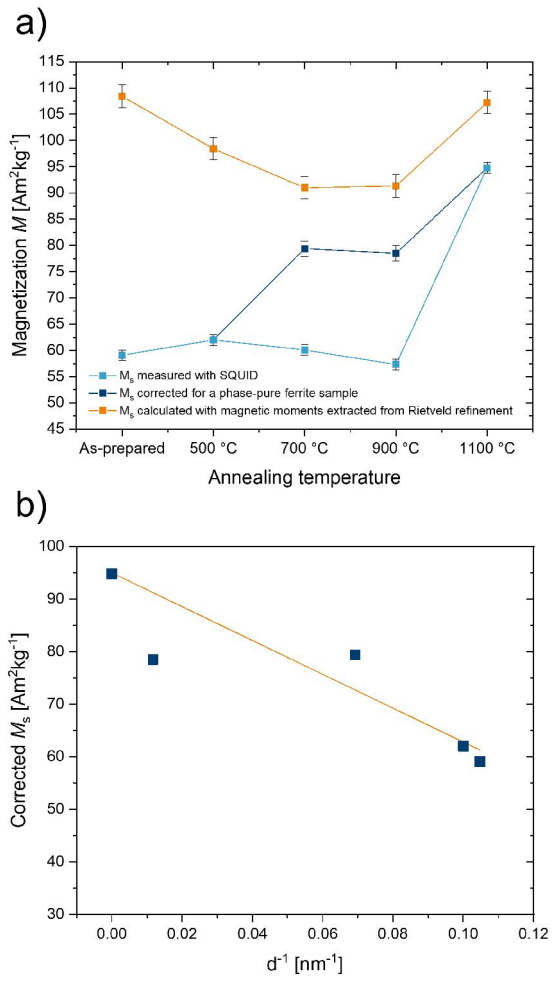

Figure 6: a) Magnetic properties of $Mn_{0.6}Zn_{0.2}Fe_{2.2}O_4$. For the samples annealed at 700 °C and 900 °C, the calculated value for a theoretical phase pure ferrite sample is displayed additionally. Moreover, the saturation magnetizations extracted from Rietveld refinements are shown, b) Correlation between the corrected saturation magnetization (blue squares) and the inverse diameter of the crystallites, with a linear fit (orange line). For the linear fit, the y-axis intercept was fixed to M_s *of the sample annealed at 1100 °C, being the bulk value of* M_s*. This graph illustrates the dependence of the magnetic properties on the surface area. The full hysteresis curves can be found in Figure S6 in the Supporting Information.*

The observed change of the magnetic properties does not reflect in the cation migration occuring during the annealing. This is not surprising as the non-magnetic Zn(II) stays on tetrahedral sites, while Mn and Fe swap positions. With Mn(II) and Fe(III) being isoelectronic, no change of M_s is expected upon a redistribution of those cations. The cause for the change of M_s during the annealing are therefore microstructural effects.

The enhancement of M_s with increasing annealing temperature can be explained the surface-to-volume ratio of the crystallites decreasing. Thus, the broken bonds and reduction of long-range order at the surface layer leading to spin canting at the crystallites' surface become less significant, increasing the overall M_s of the sample.[21,45,46] Assuming a constant thickness of the surface layer exhibiting spin canting, changes of the surface-to-volume ratio of the crystallites should yield a linear trend of M_s depending on the inverse crystallite size (Figure 6b). This fits well for the samples solely containing the spinel ferrite phase, indicating that surface effects play a major role for the modification of the M_s. However, deviations of the samples annealed at 700 and 900 C from the linear trend are observed, likely due to other, surface-independent effects, such as the lower Fe content in the spinel phase as the α-Fe_2O_3 phase evolves.

Magnetic moments were moreover extracted from the Rietveld refinement (Figure 6a and Table 1). At annealing temperatures of 700 °C and above, the refined moments confirm the same trend of M_s as measured with the SQUID. However, when annealed at temperatures below 700 °C, the refined magnetic moment of the samples decreases with increasing temperature, while the M_s measured with the SQUID increases. This trend could be explained by the crystallites that were annealed at temperatures below 700 °C being superparamagnetic. The neutron beam interacts on a shorter time scale (10^{-14} s) with the sample, which is slower than the fluctuation of the magnetic moment in a superparamagnet, while in the physical property measurement, the moment is averaged over a comparably large time span (seconds). Therefore, the moment extracted from a NPD pattern may appear larger, while the corresponding measured M_s is significantly lower. In the literature, the value for the critical crystallite size of superparamagnetism for Fe_3O_4 is 13 nm.[47] The magnetocrystalline anisotropy (K_u) of Fe_3O_4, which determines the critical superparamagnetic size, should be comparable to that of Mn-Zn ferrites. Therefore, it is likely that the crystallite growth occuring between 500 and 700 °C renders the crystallite size above the critical limit for superparamagnetism, and thus increases the measured M_s. Moreover, especially the as-prepared sample and those annealed at comparably low temperatures may still contain some amorphous or unreacted material, decreasing the saturation magnetization measured with the SQUID.

A similar crystallite size dependent change of M_s has not only been observed for Mn-containing spinel ferrites,[21,45,46] but also frequently for $CoFe_2O_4$ and $Co_{1-x}Zn_xFe_2O_4$.[11,48,49] One of those studies also described

changes of M_s depending on the annealing atmosphere, possibly stemming from cation redistributions.[49] This illustrates that both controlled treatment and detailed characterization of spinel ferrite samples are paramount for a reliable determination and understanding of the origin of the magnetic properties.

Conclusions

Temperature treatment has a major effect on the microstructure and cation distribution in spinel ferrites and subsequently, on the material's magnetic properties. In this study, we show how the annealing of $Mn_{0.6}Zn_{0.2}Fe_{2.2}O_4$ nanoparticles followed by controlled cooling in the furnace leads to materials with distinct structural properties depending on the annealing temperature. This way, a massive increase of the saturation magnetization by more than 60% to a value of 95(1) Am^2kg^{-1} was realized. α-Fe_2O_3 appears as an impurity phase at 700 and 900 °C in quantities around 25%, but the weight fraction almost disappears when annealed at 1100 °C. Two temperature regimes are identified for changes in the structural properties of the spinel ferrite. Below *ca*. 700 °C cation redistribution occurs, with Mn(II) ions moving to the tetrahedral sites, whereas significant crystallite growth arises above 700 °C. The cation distribution is therefore not a size effect, but it is strongly defined by the sample's thermal history, including cooling rates. Zn(II) remains in a normal distribution, while Mn(II) migrates from 80(7)% occupying octahedral sites to a normal distribution, exclusively occupying tetrahedral sites. This effect is corroborated by changes in the oxygen position within the spinel structure. The magnetic properties were not affected by the cation redistribution, as Mn(II) and Fe(III) are isoelectronic. Thus, changes in the saturation magnetization are introduced by surface effects such a spin canting, being more pronounced in smaller particles with larger surface-to-bulk ratio.

These results show how a thermal treatment of spinel ferrites can be used as a handle to adjust the microstructure and cation distribution in nanoparticles and therefore to synthesize spinel ferrites with enhanced magnetic properties.

Supporting Information

- Diffractograms showing the fit of the Rietveld refinement of PXRD and NPD patterns of the as-prepared sample and samples annealed at 500 °C, 700 °C and 1100 °C, tables with refined parameters, additional TEM images, EDS spectra and STEM-HAADF images for two samples (as-prepared and annealed at 1100 °C), including tables for the determined composition, hysteresis curves from the SQUID measurement

Acknowledgements

The authors are grateful for financial support from the European Commission through the H2020 project AMPHIBIAN (H2020-NMBP-2016-720853). Support from the Danish National Research Foundation (Center

for Materials Crystallography, DNRF-93), and the Danish Center for Synchrotron and Neutron Science (DanScatt) is gratefully acknowledged. We would also like to acknowledge the assistance from instrument staff; Lukas Keller at SINQ, PSI, Switzerland and Thomas Hansen, at ILL, Grenoble, France. Affiliation with the Center for Integrated Materials Research (iMAT) at Aarhus University is gratefully acknowledged by JH, PGG, MSM and MC. JH acknowledges affiliation with the Sino-Danish Center for Education and Research (SDC).

Conflict of Interest

The authors declare no competing financial interest.

References

(1) Jang, J.-t.; Nah, H.; Lee, J.-H.; Moon, S. H.; Kim, M. G.; Cheon, J. Critical enhancements of MRI contrast and hyperthermic effects by dopant-controlled magnetic nanoparticles. *Angew. Chem.* **2009**, *48*, 1234–1238.

(2) Hee Kim, E.; Sook Lee, H.; Kook Kwak, B.; Kim, B.-K. Synthesis of ferrofluid with magnetic nanoparticles by sonochemical method for MRI contrast agent. *J. Magn. Magn. Mater.* **2005**, *289*, 328–330.

(3) Hergt, R.; Dutz, S.; Müller, R.; Zeisberger, M. Magnetic particle hyperthermia: nanoparticle magnetism and materials development for cancer therapy. *J. Phys.: Condens. Matter* **2006**, *18*, S2919-S2934.

(4) Sun, C.; Lee, J. S. H.; Zhang, M. Magnetic nanoparticles in MR imaging and drug delivery. *Adv. Drug Deliv. Rev.* **2008**, *60*, 1252–1265.

(5) Lu, A.-H.; Schmidt, W.; Matoussevitch, N.; Bönnemann, H.; Spliethoff, B.; Tesche, B.; Bill, E.; Kiefer, W.; Schüth, F. Nanoengineering of a Magnetically Separable Hydrogenation Catalyst. *Angew. Chem.* **2004**, *116*, 4403–4406.

(6) Stoppels, D. Developments in soft magnetic power ferrites. *J. Magn. Magn. Mater.* **1996**, *160*, 323–328.

(7) Kneller, E. F.; Hawig, R. The exchange-spring magnet: a new material principle for permanent magnets. *IEEE Trans. Magn.* **1991**, *27*, 3588-3560.

(8) Zeng, H.; Li, J.; Liu, J. P.; Wang, Z. L.; Sun, S. Exchange-coupled nanocomposite magnets by nanoparticle self-assembly. *Nature* **2002**, *420*, 395–398.

(9) Gorter E. W. Magnetization in ferrites; saturation magnetization of ferrites with spinal structure. *Nature* **1950**, *165*, 798–800.

(10) Chikazumi, S. *Physics of ferromagnetism*, 2. ed.; The international series of monographs on physics 94; Oxford Univ. Press: Oxford, 2010.

(11) Albino, M.; Fantechi, E.; Innocenti, C.; López-Ortega, A.; Bonanni, V.; Campo, G.; Pineider, F.; Gurioli, M.; Arosio, P.; Orlando, T.*; et al.* Role of Zn 2+ Substitution on the Magnetic, Hyperthermic, and Relaxometric Properties of Cobalt Ferrite Nanoparticles. *J. Phys. Chem. C* **2019**, *123*, 6148–6157.

(12) Hölscher, J.; Andersen, H. L.; Saura-Múzquiz, M.; Garbus, P. G.; Christensen, M. Correlation between microstructure, cation distribution and magnetism in Ni_1-xZnxFe_2O_4 nanocrystallites. *CrystEngComm* **2020**, *22*, 515–524.

(13) Andersen, H. L.; Granados-Miralles, C.; Saura-Múzquiz, M.; Stingaciu, M.; Larsen, J.; Søndergaard-Pedersen, F.; Ahlburg, J. V.; Keller, L.; Frandsen, C.; Christensen, M. Enhanced intrinsic saturation magnetization of Zn x Co 1−x Fe 2 O 4 nanocrystallites with metastable spinel inversion. *Mater. Chem. Front.* **2019**, *3*, 668–679.

(14) Momma, K.; Izumi, F. VESTA 3 for three-dimensional visualization of crystal, volumetric and morphology data. *J. Appl. Crystallogr.* **2011**, *44*, 1272–1276.
(15) Feng, J.; Guo, L.-Q.; Xu, X.; Qi, S.-Y.; Zhang, M.-L. Hydrothermal synthesis and characterization of Mn1−xZnxFe2O4 nanoparticles. *J. Phys.: Conf. Ser.* **2007**, *394*, 100–103.
(16) Hessien, M. M.; Rashad, M. M.; El-Barawy, K.; Ibrahim, I. A. Influence of manganese substitution and annealing temperature on the formation, microstructure and magnetic properties of Mn–Zn ferrites. *J. Magn. Magn. Mater.* **2008**, *320*, 1615–1621.
(17) Arulmurugan, R.; Vaidyanathan, G.; Sendhilnathan, S.; Jeyadevan, B. Mn–Zn ferrite nanoparticles for ferrofluid preparation: Study on thermal–magnetic properties. *J. Magn. Magn. Mater.* **2006**, *298*, 83–94.
(18) Sickafus, K. E.; Wills, J. M.; Grimes, N. W. Structure of Spinel. *J. Am. Ceram. Soc.* **1999**, *82*, 3279–3292.
(19) Sawatzky, G. A.; van der Woude, F.; Morrish, A. H. Mössbauer Study of Several Ferrimagnetic Spinels. *Phys. Rev.* **1969**, *187*, 747–757.
(20) Upadhyay, C.; Verma, H. C.; Rath, C.; Sahu, K. K.; Anand, S.; Das, R. P.; Mishra, N. C. Mössbauer studies of nanosize Mn1−xZnxFe2O4. *J. Alloys. Compd.* **2001**, *326*, 94–97.
(21) Chen; Sorensen; Klabunde; Hadjipanayis; Devlin; Kostikas. Size-dependent magnetic properties of MnFe2O4 fine particles synthesized by coprecipitation. *Phys. Rev. B* **1996**, *54*, 9288–9296.
(22) Verwey, E. J. W.; Heilmann, E. L. Physical Properties and Cation Arrangement of Oxides with Spinel Structures I. Cation Arrangement in Spinels. *J. Chem. Phys.* **1947**, *15*, 174–180.
(23) Andersen, H. L.; Saura-Múzquiz, M.; Granados-Miralles, C.; Canévet, E.; Lock, N.; Christensen, M. Crystalline and magnetic structure-property relationship in spinel ferrite nanoparticles. *Nanoscale* **2018**, *10*, 14902–14914.
(24) Kamiyama, T.; Haneda, K.; Sato, T.; Ikeda, S.; Asano, H. Cation distribution in ZnFe2O4 fine particles studied by neutron powder diffraction. *Solid State Commun.* **1992**, *81*, 563–566.
(25) Carta, D.; Casula, M. F.; Falqui, A.; Loche, D.; Mountjoy, G.; Sangregorio, C.; Corrias, A. A Structural and Magnetic Investigation of the Inversion Degree in Ferrite Nanocrystals MFe 2 O 4 (M = Mn, Co, Ni). *J. Phys. Chem. C* **2009**, *113*, 8606–8615.
(26) Antic, B.; Perovic, M.; Kremenovic, A.; Blanusa, J.; Spasojevic, V.; Vulic, P.; Bessais, L.; Bozin, E. S. An integrated study of thermal treatment effects on the microstructure and magnetic properties of Zn-ferrite nanoparticles. *J. Phys.: Condens. Matter* **2013**, *25*, 86001.
(27) Jirák, Z.; Vratislav, S. Temperature dependence of distribution of cations in MnFe2O4. *Czech. J. Phys.* **1974**, *24*, 642–647.
(28) Gabal, M. A.; Ata-Allah, S. S. Concerning the cation distribution in MnFe2O4 synthesized through the thermal decomposition of oxalates. *J. Phys. Chem. Solids* **2004**, *65*, 995–1003.
(29) Figueroa, S. J. A.; Stewart, S. J. First XANES evidence of a disorder-order transition in a spinel ferrite compound: nanocrystalline ZnFe2O4. *J. Synchrotron Radiat.* **2009**, *16*, 63–68.
(30) Ichikawa, R. U.; Parra, J. P. R. L. L.; Vallcorba, O.; Peral, I.; Yoshito, W. K.; Saeki, M. J.; Turrillas, X.; Martinez, L. G. Cation distribution of Mn-Zn ferrite nanoparticles using pair distribution function analysis and resonant X-ray scattering. *EPL* **2018**, *124*, 56001.
(31) Xiao, L.; Zhou, T.; Meng, J. Hydrothermal synthesis of Mn–Zn ferrites from spent alkaline Zn–Mn batteries. *Particuology* **2009**, *7*, 491–495.
(32) Antic, B.; Kremenović, A.; Nikolic, A. S.; Stoiljkovic, M. Cation Distribution and Size-Strain Microstructure Analysis in Ultrafine Zn−Mn Ferrites Obtained from Acetylacetonato Complexes. *J. Phys. Chem. B* **2004**, *108*, 12646–12651.
(33) Shahane, G. S.; Zipare, K. V.; Bandgar, S. S.; Mathe, V. L. Cation distribution and magnetic properties of Zn2+ substituted MnFe2O4 nanoparticles. *J. Mater. Sci.: Mater. Electron.* **2017**, *28*, 4146–4153.

(34) Schefer, J.; Fischer, P.; Heer, H.; Isacson, A.; Koch, M., Thut, R. A versatile double-axis multicounter neutron powder diffractometer. *Nucl. Instrum. Methods Phys. Res. A* **1990**, 477–485.
(35) Orench, I. P.; Clergeau, J. F.; Martínez, S.; Olmos, M.; Fabelo, O.; Campo, J. The new powder diffractometer D1B of the Institut Laue Langevin. *J. Phys.: Conf. Ser.* **2014**, 12003.
(36) Christensen, M.; Ahlburg, J. V.; Julian Fernandez, C. de; Gjørup, F.; Hansen, T.; Hölscher, J.; Mørch, M. *Following crystallite morphology and magnetization during sintering of compacted strontium hexaferrite nano-platelets*, Institut Laue-Langevin (ILL), doi: 10.5291/ILL-DATA.1-04-146, 2019.
(37) Rodriguez-Carvajal, J. Recent advances in magnetic structure determination by neutron powder diffraction. *Physica B* **1993**, 55–69.
(38) Cullity, B. D.; Graham, C. D. *Introduction to magnetic materials*, 2nd ed.; Wiley: Hoboken, N.J, 2009.
(39) Hu, P.; Yang, H.-b.; Pan, D.-a.; Wang, H.; Tian, J.-j.; Zhang, S.-g.; Wang, X.-f.; Volinsky, A. A. Heat treatment effects on microstructure and magnetic properties of Mn–Zn ferrite powders. *J. Magn. Magn. Mater.* **2010**, *322*, 173–177.
(40) Bonsdorf, G. Stability region and oxygen stoichiometry of manganese ferrite. *Solid State Ion.* **1998**, *110*, 73–82.
(41) Shannon, R. D. Revised effective ionic radii and systematic studies of interatomic distances in halides and chalcogenides. *Acta Crystallogr. A* **1976**, *32*, 751–767.
(42) Zhang, Z. J.; Wang, Z. L.; Chakoumakos, B. C.; Yin, J. S. Temperature Dependence of Cation Distribution and Oxidation State in Magnetic Mn−Fe Ferrite Nanocrystals. *J. Am. Chem. Soc.* **1998**, *120*, 1800–1804.
(43) Wei, C.; Feng, Z.; Baisariyev, M.; Yu, L.; Zeng, L.; Wu, T.; Zhao, H.; Huang, Y.; Bedzyk, M. J.; Sritharan, T.*; et al.* Valence Change Ability and Geometrical Occupation of Substitution Cations Determine the Pseudocapacitance of Spinel Ferrite XFe 2 O 4 (X = Mn, Co, Ni, Fe). *Chem. Mater.* **2016**, *28*, 4129–4133.
(44) Özdemir, Ö.; Dunlop, D. J. Hysteresis and coercivity of hematite. *J. Geophys. Res. B* **2014**, *119*, 2582–2594.
(45) van der Zaag, P. J.; Ruigrok, J. J. M.; Noordermeer, A.; van Delden, M. H. W. M.; Por, P. T.; Rekveldt, M. T.; Donnet, D. M.; Chapman, J. N. The initial permeability of polycrystalline MnZn ferrites: The influence of domain and microstructure. *J. Appl. Phys.* **1993**, *74*, 4085–4095.
(46) Berkowitz, A. E.; Schuele, W. J.; Flanders, P. J. Influence of Crystallite Size on the Magnetic Properties of Acicular γ-Fe 2 O 3 Particles. *J. Appl. Phys.* **1968**, *39*, 1261–1263.
(47) Coey, J. M. D. *Magnetism and Magnetic Materials*; Cambridge University Press, 2012.
(48) Soleimani, H.; Ahmad Latiff, N. R.; Zaid, H. M.; Yahya, N.; Sadrolhosseini, A. R.; Adil, M. Effect of synthesis parameters on cobalt ferrite saturation magnetization. *J. Magn. Magn. Mater.* **2018**, *1123*, 12017.
(49) Schmidt, M.; Andersen, H. L.; Granados-Miralles, C.; Saura-Múzquiz, M.; Stingaciu, M.; Christensen, M. Tuning the size and magnetic properties of $Zn_xCo_{1-x}Fe_2O_4$ nanocrystallites. *Dalton Trans.* **2016**, *45*, 6439–6448.

For Table of Contents Only

The saturation magnetization of magnetic Mn-Zn ferrites is increased by more than 60% using thermal treatment. Robust combined Rietveld refinement of powder X-ray and neutron diffraction data reveal that a reordering of the cations and a modification of the microstructure take place during the annealing step, the extent of which can be controlled by the annealing temperature.